Iron Dissolution from Goethite (α-FeOOH) Surfaces in Water by Ab Initio Enhanced Free-Energy Simulations

Konstantin Klyukin,[†] Kevin M. Rosso,[‡] and Vitaly Alexandrov*,[†,§]

[†]Department of Chemical and Biomolecular Engineering and [§]Nebraska Center for Materials and Nanoscience, University of Nebraska-Lincoln, Lincoln, Nebraska 68588, United States
[‡]Pacific Northwest National Laboratory, Physical Sciences Division, Richland 99354, United States

S *Supporting Information*

ABSTRACT: Dissolution of redox-active metal oxides plays a key role in a variety of phenomena, including (photo)-electrocatalysis, degradation of battery materials, corrosion of metal oxides, and biogeochemical cycling of metals in natural environments. Despite its widespread significance, mechanisms of metal-oxide dissolution remain poorly understood on the atomistic level. This study is aimed at elucidating the long-standing problem of iron dissolution from Fe(III)-oxide, a complex process involving coupled hydrolysis, surface protonation, electron transfer, and metal−oxygen bond cleavage. We examine the case of goethite (α-FeOOH), a representative phase, bearing structural similarities with many other metal (hydr)oxides. By employing quantum molecular dynamics simulations (metadynamics combined with the Blue Moon ensemble approach), we unveil the mechanistic pathways and rates of both nonreductive and reductive dissolution of iron from the (110) and (021) goethite facets in aqueous solutions at room temperature. Our simulations reveal the interplay between concerted internal (structural) and external (from solution) protonations as essential for breaking Fe−O bonds as well as for stabilizing intermediate configurations of dissolving Fe. We demonstrate specifically how Fe(III) reduction to Fe(II) yields higher dissolution rates than the proton-mediated pathway, whereas the most rapid dissolution is expected for these two processes combined, in agreement with experiments.
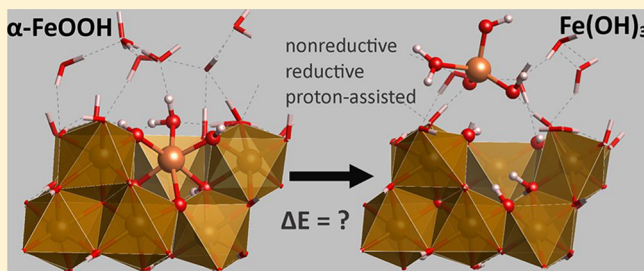
INTRODUCTION

Material dissolution is pervasive to many areas of science, playing both beneficial and detrimental roles in various phenomena. Iron (hydr)oxides are an important family of redox-active compounds for which iron dissolution has been a focal point of research efforts in the last few decades. Iron is the most abundant redox-active element on the Earth's crust, and its global biogeochemical cycling is coupled to a variety of processes in natural environments (atmosphere, hydrosphere, and lithosphere).[1−4] Iron dissolution also plays a critical role in many technologies including photo-assisted degradation of catalysts,[5−8] metal dissolution from battery materials,[9−11] as well as corrosion of metal oxides and steel.[12]

Despite years of experimental research, because of its complexity, the atomistic details of redox-active metal oxide dissolution in aqueous solutions remain elusive. In the case of iron (hydr)oxides, although a wealth of macroscopic kinetics data are available for multiple dissolution mechanisms (acidic, reductive, acidic/reductive, and ligand-assisted), the resulting mechanistic models remain purely speculative. There is lack of microscopic data for well-characterized systems including, for example, surface-specific dissolution rates. On the basis of macroscopic kinetics data, however, it can be expected that much of the mechanistic detail is generalizable across systems. For example, the elementary metal-ion detachment steps are

likely to be analogous across a variety of metal (hydr)oxides (M = Fe, Mn, Cr, etc.) featuring similar M−O octahedral topology, except for the specific role of extra protonation or metal reduction.

Specifically for iron oxides, a recently proposed "redox-driven conveyor belt" mechanism[13] suggests that oxidative Fe^{2+} uptake occurs at one crystal face of an iron oxide, whereas the reductive Fe^{3+} dissolution takes place at a different face, and these processes are driven by potential gradients existing between the faces and electron transport.[14] In the case of goethite (α-FeOOH), this mechanism implies that nanoparticles preferentially grow on the sides [primarily (110) and (010) facets, *Pbnm* space group], whereas iron dissolution predominantly occurs from the goethite tips [mostly (021) and (432) facets].[15] It was recently demonstrated computationally that Fe(II) release should be the rate-limiting step in the overall goethite recrystallization process.[16]

One experimental challenge in studying dissolution of oxide materials in aqueous environments is that dissolution rates depend strongly on multiple interrelated factors such as Fe(III) reduction, solution pH, crystallite size and morphology,

crystallinity, and structural defects. This makes it difficult to deconvolute various effects experimentally and provide a unified picture of the dissolution mechanism. In this regard, first-principles simulations offer an opportunity to investigate various steps on the atomic level with no adjustable parameters. Although the problem of material dissolution has long attracted a great deal of theoretical attention,[17−19] only recently, ab initio molecular dynamics (AIMD)-based approaches have become feasible for simulating rare events such as dissolution under realistic experimental conditions (dynamics, explicit solvent, and temperature).[11,20]

There are two major mechanisms of iron dissolution: (i) reductive dissolution when structural iron dissolves as Fe^{2+} (i.e., ferrous iron) species and (ii) acidic dissolution when it dissolves as Fe^{3+}. It is established that the reductive mechanism yields higher dissolution rates on the basis that reduction of structural Fe^{3+} (chemically,[12] photochemically,[4] or microbially[21,22]) weakens lattice Fe−O bonds, thereby promoting detachment of Fe^{2+} species into solution.

It is also well-understood that the release of structural iron is also facilitated by protonation of surface oxygen atoms at acidic pH. These protonation reactions can operate alone or in concert with reduction, further destabilizing the Fe−O bonds and lowering the activation barrier for iron dissolution. Such proton-assisted dissolution leads to a strong pH dependence of the dissolution rate generally.[12] It was measured that the rate of goethite dissolution can be several orders of magnitude larger for reductive dissolution than for the proton-mediated mechanism alone,[23] and the reductive dissolution rate is enhanced in acidic environments. However, the exact reasons on the atomistic scale for this redox-based acceleration of the dissolution rate remain undetermined, in particular, how protonation couples with reduction to yield facile Fe−O bond dissociation.

In recent years, accelerated AIMD approaches have been increasingly applied to sample reaction configurations to predict free-energy diagrams that explicitly include solvent and entropy effects for a variety of chemical processes.[11,17,24] In the case of dissolution, there have been a number of first-principles investigations employing rare-event simulations that focused on metal dissolution from complex oxide surfaces, especially in the context of degradation of lithium-ion battery cathode materials.[11,20] These approaches enable exploration of dissolution pathways at the fully quantum-mechanical footing, taking into account important proton transfer and solvent rearrangement. The latter processes are known to play critical roles in determining both rates and pathways of chemical reactions in aqueous environments.[24,25]

COMPUTATIONAL METHODOLOGY

In this paper, we undertake detailed AIMD-based simulations of iron dissolution from goethite (110) and (021) surfaces (Figure 1), which are representative of the goethite nanoparticle edges and caps, respectively.[26−28] We employ density functional theory (DFT)-based Born−Oppenheimer molecular dynamics (BOMD) simulations coupled with metadynamics and Blue Moon ensemble techniques, as implemented in the VASP code.[29] All simulations are performed employing the Perdew−Burke−Ernzerhof functional along with the projector-augmented wave formalism. Generalized gradient approximation + U approach with U_{eff} = 5 eV was applied to localize the charge on Fe ions in the goethite structure following a series of previous studies.[26−28] Comparison between DFT + U, B3LYP,
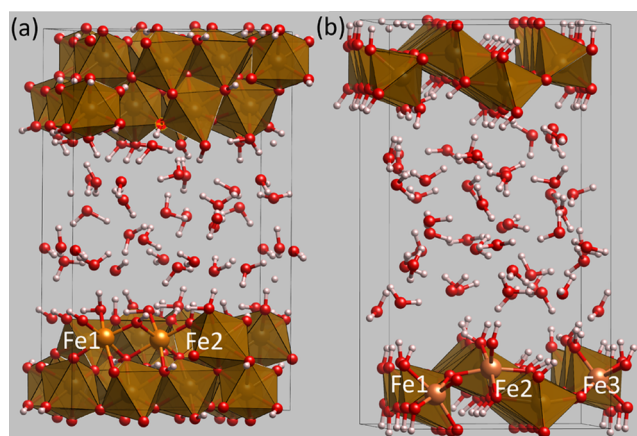

Figure 1. Side view of the supercell models for the (021) (a) and (110) (b) goethite hydroxylated surfaces. Symmetrically inequivalent topmost Fe atoms investigated for dissolution are denoted.

M06, and M06L results for deprotonation energies of $Fe^{3+}(H_2O)_6$ made by Leung and Criscenti[30] also suggest that DFT + U predictions are sufficiently accurate to reproduce experimental pK_a data for goethite surfaces. To drive electron localization to either the Fe^{2+} or Fe^{3+} state, we set the initial magnetic moments on Fe ions to correspond to a desired configuration: Fe^{2+}—3.8 μ_B and Fe^{3+}—4.3 μ_B. A 1.0 fs time step in the BOMD simulations and a hydrogen mass of 2 amu were applied. Our additional test simulations with the H mass of 3 amu and van der Waals corrections (DFT-D3 method of Grimme) demonstrated that our choice of parameters is reasonable and does not affect dissolution barriers significantly, as detailed in the Supporting Information (Figure S15). BOMD simulations used only the Γ point of the Brillouin zone with no symmetry imposed. The Nose−Hoover thermostat[31,32] was used to keep the simulation temperature around 300 K.

In estimating the dissolution free-energy barriers, we do not solely rely on the metadynamics method because dissolution reactions are characterized by multiple bond-breaking and bond-healing events that make accurate evaluation of the free-energy barriers challenging. Instead, we use metadynamics trajectories as the energetically favorable reaction pathways for subsequent Blue Moon ensemble simulations to allow more accurate determination of metastable intermediate states and associated bond-breaking activation barriers. Thus, metadynamics simulations are first applied to explore the free-energy landscape and identify energetically favorable dissolution pathways, and then each Fe−O bond breaking event is sampled separately utilizing the Blue Moon ensemble method by using a set of collective variables specific to each region. A number of preliminary metadynamics trajectories were generated to show that the Gaussian hill height of 0.07 eV and the width of 0.15 Å are reasonable simulation parameters. A set of windows along each reaction pathway identified by metadynamics is selected for subsequent thermodynamic integration calculations, as described in detail in the Supporting Information for each case. Configurations in each window are additionally equilibrated during 2−3 ps, and simulations of 2−10 ps are carried out to collect and average the force along the reaction direction. The free-energy gradient curves are computed along the reaction coordinates defined as the distances between Fe and oxygen atoms from its first

coordination sphere. The use of thermodynamic integration calculations allows us to study activation barriers more systematically and distinguish contributions from different factors (such as protonation and reduction) at each dissolution step.

The standard uncertainty in free-energy gradients is estimated using the block average method.[33] A similar approach has been previously applied to obtain the free-energy profiles for Mn(II) dissolution from spinel $Li_xMn_2O_4$ (001) surfaces.[11,20] As stated above, in our calculations, we use 2 ps trajectories to collect the free-energy gradient and compute the average. To estimate the error, we consider a longer trajectory of 10 ps and accumulate 5 blocks of 2 ps each. Then, we calculate the standard deviation for the energy gradient, after which the linear error propagation theory is used to calculate the uncertainty for activation energy barriers, as shown in Figure 2. Thus, the activation energy for the first step
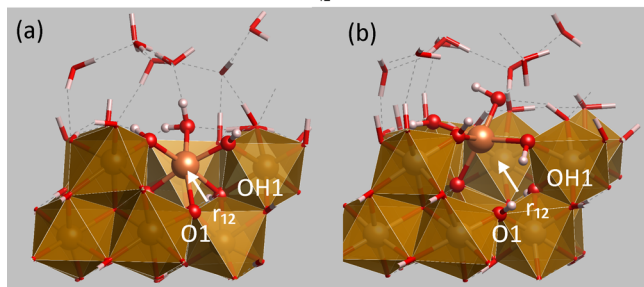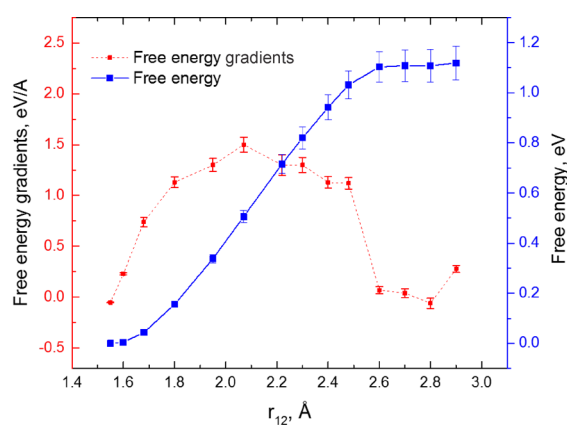

Figure 2. Free-energy gradients (left-hand scale) and integrated free energy (right-hand scale) along with the corresponding uncertainties vs reaction coordinate r_{12} (the distance between Fe atom and the center of bond between atom O1 and oxygen atom from OH1) for Fe^{3+} dissolution from the Fe2 site of the (021) surface between (a) and (b) intermediate states.

of Fe2 dissolution through the nonreductive mechanism is 1.11 ± 0.06 eV, which corresponds to an error of 5%. Because the total dissolution barrier is about twice larger than the first dissolution step, the error is cumulative, but the gradients are decreasing; we can estimate that the overall error for the total activation barrier should not exceed 10%.

The (110) and (021) goethite surfaces (in *Pbnm* setting) are modeled using periodic slabs with a vacuum gap of 10 Å and surface cells of 11.04×12.16 Å^2 for the (110) surface and 9.24×11.73 Å^2 for the (021) surface (see Figure 1). The basic properties of these goethite surfaces such as thermodynamic stability, hydroxylation, and surface interactions with various solution species were previously explored in a number of first-principles studies.[26,27,30,34−38] Here, we analyze the dissolution

of all symmetrically inequivalent topmost Fe atoms for both facets using simulation cells shown in Figure 1. The nonreductive mechanism corresponds to the dissolution of a structural Fe^{3+} ion, whereas the reductive pathway is the case in which one Fe^{2+} polaron created on the goethite surface by reduction is being dissolved to the solution.

■ RESULTS AND DISCUSSION

We first analyze iron dissolution from the Fe2 site of the (021) surface and from the Fe1 site of the (110) surface. All other cases are described in detail in the Supporting Information, with all estimated free-energy barriers being summarized in Table 1. Figure 3 shows the free-energy profiles for iron

Table 1. Summarized Activation Barriers (in eV) for Fe^{2+}/Fe^{3+} Atom Dissolution from the (021)/(110) Goethite/Water Interface[a]

surface	site	Fe^{3+}	Fe^{3+} proton-assisted	Fe^{2+} reductive
021	Fe1	1.81	1.09	1.02
	Fe2	1.89	1.18	1.12
110	Fe1	2.89	1.71	1.69
	Fe2	3.38	1.93	1.91
	Fe3	2.09	1.38	1.24

[a]The positions of Fe atoms are labeled in accordance with Figure 1.

dissolution from the Fe2 site on the (021) facet via different mechanisms (nonreductive, reductive, and proton-assisted). The associated metastable intermediate structures are shown only for the Fe^{3+} dissolution (Figure 3, right). In this case, the first bond-breaking event (from state a to b) is characterized by almost simultaneous breaking of the two bonds—first Fe−OH and then Fe−O (see the metadynamics trajectory in the Supporting Information). Upon breaking of these two bonds, the dissolving Fe^{3+} ion forms a new bond with the nearest surface OH group, whereas the H_2O molecules bonded to this Fe^{3+} ion dissociates to give another OH group (see Figure 3, state b). At the same time, the structural O atom left behind becomes protonated by a structural proton from the nearby OH group. Then, the third Fe−O bond breaks leading to the intermediate state c. The next two states (d and e) involve the breaking of two Fe−OH bonds that takes place almost simultaneously with a very small activation barrier. First, the bond between the dissolving Fe^{3+} and structural OH is broken (state d), and then another structural OH bound to the outgoing Fe^{3+} ion detaches from the structural Fe^{3+} (state e) and leaves the surface together with the dissolving Fe^{3+} ion. Concurrently, an H_2O molecule from the solution binds to the dissolving Fe^{3+} ion and subsequently hydrolyzes, resulting in one more OH group. During the next step (from state e to f), the remaining bond between the dissolving Fe^{3+} and structural OH is broken. Thus, Fe^{3+} leaves the surface as $Fe(OH)_3$, and within a short period of time, it binds to an additional H_2O molecule from the solution to become $Fe(OH)_3 \cdot H_2O$ (final state f).

In the case of Fe^{2+} dissolution from the same Fe2 surface site of the (021) facet, the sequence of the bond-breaking events observed in our simulations is very similar to the Fe^{3+} case described above. The difference is that upon transitioning from state a to b when two Fe−O bonds are being broken, Fe^{2+} does not form a new Fe−OH bond as was in the case of Fe^{3+}, which can be explained by its lower oxidation state. When the next Fe−O bond breaks, however, this new Fe−OH bond is formed
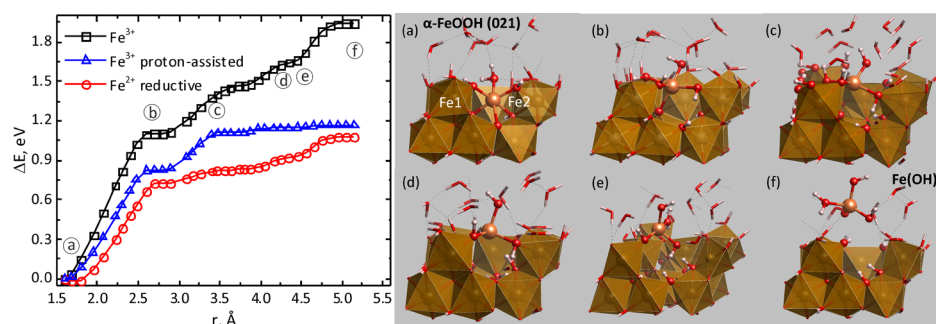
Figure 3. Free-energy profiles of iron dissolution from the Fe2 site of the (021) surface for the reductive (as Fe^{2+}) and nonreductive (as Fe^{3+} at neutral and acidic pH) mechanisms. (a−f) correspond to the initial, final, and intermediate metastable structures along the dissolution pathway shown on the right for dissolution of iron as Fe^{3+}. Every bond-breaking event (4 total) is sampled using 10 windows of 2 ps long each in the Blue Moon ensemble simulations.
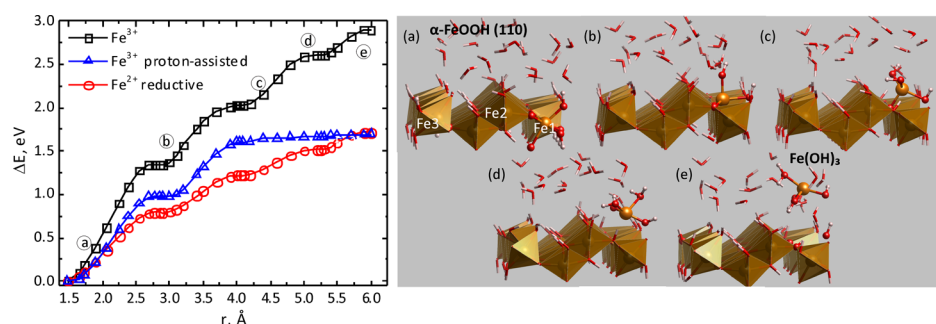

Figure 4. Free-energy profiles of iron dissolution from the Fe1 site of the (110) surface for the reductive (as Fe^{2+}) and nonreductive (as Fe^{3+} at neutral and acidic pH) mechanisms. (a−e) correspond to the initial, final, and intermediate metastable structures along the dissolution pathway shown on the right for dissolution of iron as Fe^{3+}. Every bond-breaking event (4 total) is sampled using 10 windows of 2 ps long each in the Blue Moon ensemble simulations.

so that the final state c for both Fe^{2+} and Fe^{3+} is chemically equivalent. Eventually, Fe^{2+} dissolves as $Fe(OH)_2·H_2O$ species (final state f).

To evaluate the impact of solution pH on dissolution rates, we consider the case when all Fe−O bonds that are being broken during dissolution of structural Fe^{3+} are subsequently protonated for each intermediate state (see the Supporting Information for details). This allows us to estimate the upper limit of the rates for proton-assisted nonreductive dissolution without going into the details of the protonation kinetics and mechanisms for the corresponding structural oxygen species. Although surface stability may also change as a function of pH, which in turn may play a role for accurate prediction of dissolution kinetics,[39] we believe that our approach is appropriate to demonstrate the critical role of solvated protons on iron dissolution.

It is here noted that although the propensity for protonation of subsurface and surface Fe−OH groups should increase at low pH, the equilibrium of water dissociation, which stabilizes iron intermediates as seen in our simulations, is shifted toward H_2O and thus acts as a competing effect against Fe detachment from the surface. This also suggests that dissolution may entail the formation of a disordered iron-oxide phase on the surface. In fact, amorphous mixed-valence iron precipitates were observed experimentally during reductive dissolution of Fe(III) (hydr)oxides.[40]

Energetically, it is seen from the Fe^{3+} free-energy profile in Figure 3 that the first dissolution step (from a to b) comprised of two bond-breaking events accounts for the largest portion of the activation barrier (∼1.1 eV), whereas the whole dissolution

process (from the initial state a to the final state f) yields the total free-energy barrier of about 1.89 eV. The proton-assisted mechanism of Fe^{3+} dissolution leads to a reduction of the dissolution barrier by as much as 0.71 eV, mainly due to spontaneous breaking of external Fe−OH bonds. Overall, the lowest dissolution rate is observed for the reductive dissolution pathway that could be estimated as 1.12 eV according to Figure 3. We also note that the bond-breaking and bond-forming events observed in our simulations are consistent with the Pauling electrostatic bond strength analysis, as detailed in the Supporting Information, which shows how the dissolving Fe ions preserve local electroneutrality during the dissolution process.

For the (110) goethite surface, we consider dissolution of three topmost Fe ions (Figure 1). It is seen from Table 1 that the activation barriers for all three Fe sites across all three considered dissolution mechanisms are consistently higher than those predicted for the (021) surface. This result is in general agreement with the experimental observations of faster iron dissolution from the (021) surface that makes up the caps of the goethite nanoparticles.[15] The Fe3 site is found to exhibit the most rapid dissolution kinetics among the three surface sites. Its dissolution mechanism is determined to be similar to those found for the low-barrier Fe1 and Fe2 sites at the (021) surface. The Fe1 site of the (110) facet features one bridging OH group at the surface and has a higher activation barrier for dissolution than Fe3. The dissolution mechanism also turns out to be different, with the first metastable state b observed only after almost simultaneous breaking of three bottom Fe−O/Fe−OH bonds (see Figure 4). This state is stabilized by

nucleophilic attack by a water molecule from the solution. Then, dissolution proceeds via Fe−O bond-breaking step, leading to the intermediate state c. At the end of this bond-breaking event, Fe^{3+} catches H_2O, which then dissociates to form an OH group. In this case, the bond-breaking event is not followed by internal protonation of a surface oxygen atom, thus resulting in the relatively high activation barrier. Subsequently, the fifth Fe−O bond breaks leading to the intermediate state d. During the next step, from state d to e, the remaining bond between the dissolving Fe^{3+} and structural OH is broken. The reductive dissolution pathway features a similar sequence of bond-breaking and bond-forming events and is characterized by a considerably lower cumulative activation barrier (by about 1.2 eV) similar to the (021) case.

Whereas a more detailed description of Fe dissolution from the (110) surface is available in the Supporting Information, here we stress that the higher dissolution barriers for the (110) surface are mainly attributed to its bonding topology. Specifically, Fe2 and Fe3 sites on the (110) surface are constrained by OH bridging groups, which lead to considerably higher dissolution barriers. By contrast, the Fe1 site on (110) and the Fe2 (and Fe1) site(s) on (021) have a free −H_2O (or −OH) terminating group, which facilitates dissolution (see Table 1). It is also worth noting that sites Fe2 on the (021) surface and Fe1 on the (110) surface have a similar topology, which leads to a similar dissolution mechanism and comparable dissolution barriers for these sites.

Experimentally, the estimated activation barriers of Fe dissolution from goethite vary considerably (e.g., being ∼0.7−1.3 eV for dissolution in a strong acidic environment).[12,41−43] This variability can be explained by a number of factors affecting the dissolution rates determined for goethite nanoparticles, such as surface morphology, structural imperfections (vacancies and kinks), and various chemical compositions of aqueous solutions across different experimental studies. Qualitatively, our results reproduce the key trend observed experimentally for a number of iron oxides that reductive dissolution is the fastest mechanism of Fe dissolution followed by the nonreductive proton-assisted pathway. Quantitatively, our activation barriers are expectedly higher than those estimated from experiments because our results correspond to perfect low-index goethite surfaces free of defects; barriers may be expected to be lower for later stages of dissolution involving rough irregular surfaces such as those involved in the experiments.

CONCLUSIONS

In summary, our AIMD simulations reveal the atomistic basis for why Fe(III) reduction to Fe(II) leads to a more rapid Fe release than the acidic mechanism alone, for both (110) and (021) goethite surfaces, and why lower dissolution barriers overall are observed for the (021) facet. The results underscore the crucial role of protonation to weaken Fe−O bonds exposed to solution as well as their facet-specific topologies, underlying the acid effect of both nonreductive and reductive dissolution pathways. Specifically, we find that the largest contribution to the dissolution barrier comes from breaking the first structural Fe−O bond. Surface iron sites that are characterized by a smaller number of bridging oxygen species exhibit noticeably lower dissolution barriers as it requires breaking fewer bonds to dissolve Fe. For instance, the lowest (and comparable) dissolution barriers are determined for Fe1 and Fe2 sites of the (021) facet and Fe3 site of the (110) facet that all have similar

surface topologies featuring one oxygen species (OH or H_2O) singly bound to the dissolving Fe (terminal groups). By contrast, the Fe1 site of the (110) surface is anchored by one bridging OH group and displays a higher dissolution barrier, whereas the slowest dissolving Fe2 ions at the (110) surface is anchored by two bridging OH groups. These findings shed light on the reason why similar behavior can be observed across metal-oxide dissolution systems.

Regarding the role of pH on dissolution, our simulations reveal the importance of the balance between internal (from structural protons) and external (from solution protons) protonation. We find that although protonation of internal structural O atoms significantly weakens the Fe−O bonds and enhances dissolution, protonation of terminal Fe−O(H) groups strengthens the remaining Fe−O bonds to the surface for the dissolving Fe. In low pH environments, this process of impeding water deprotonation occurring after water attack appears to play a key role in the stabilization of intermediate states during the dissolution process.

■ ASSOCIATED CONTENT

ⓢ Supporting Information

The Supporting Information is available free of charge on the ACS Publications website at DOI: 10.1021/acs.jpcc.8b03743.

> Details on computational methodology, metadynamics, and thermodynamic integration simulations (PDF)

■ AUTHOR INFORMATION

Corresponding Author
*E-mail: valexandrov2@unl.edu. Phone: +1 402 4725323.
ORCID ⓘ
Konstantin Klyukin: 0000-0001-8325-8725
Kevin M. Rosso: 0000-0002-8474-7720
Vitaly Alexandrov: 0000-0003-2063-6914
Notes
The authors declare no competing financial interest.

■ REFERENCES

(1) Usher, C. R.; Michel, A. E.; Grassian, V. H. Reactions on mineral dust. *Chem. Rev.* **2003**, *103*, 4883−4940.

(2) Jickells, T. D.; An, Z. S.; Andersen, K. K.; Baker, A. R.; Bergametti, G.; Brooks, N.; Cao, J. J.; Boyd, P. W.; Duce, R. A.; Hunter, K. A.; et al. Global iron connections between desert dust, ocean biogeochemistry, and climate. *Science* **2005**, *308*, 67−71.

(3) Boyd, P. W.; Jickells, T.; Law, C. S.; Blain, S.; Boyle, E. A.; Buesseler, K. O.; Coale, K. H.; Cullen, J. J.; de Baar, H. J. W.; Follows, M.; et al. Mesoscale iron enrichment experiments 1993-2005: Synthesis and future directions. *Science* **2007**, *315*, 612−617.

(4) Rubasinghege, G.; Lentz, R. W.; Scherer, M. M.; Grassian, V. H. Simulated atmospheric processing of iron oxyhydroxide minerals at low H: Roles of particle size and acid anion in iron dissolution. *Proc. Natl. Acad. Sci. U.S.A.* **2010**, *107*, 6628–6633.

(5) Lyon, J. L.; Stevenson, K. J. Anomalous electrochemical dissolution and passivation of iron growth catalysts in carbon nanotubes. *Langmuir* **2007**, *23*, 11311–11318.

(6) Zou, S.; Burke, M. S.; Kast, M. G.; Fan, J.; Danilovic, N.; Boettcher, S. W. Fe (Oxy)hydroxide Oxygen Evolution Reaction Electrocatalysis: Intrinsic Activity and the Roles of Electrical Conductivity, Substrate, and Dissolution. *Chem. Mater.* **2015**, *27*, 8011–8020.

(7) Burke, M. S.; Kast, M. G.; Trotochaud, L.; Smith, A. M.; Boettcher, S. W. Cobalt-Iron (Oxy)hydroxide Oxygen Evolution Electrocatalysts: The Role of Structure and Composition on Activity, Stability, and Mechanism. *J. Am. Chem. Soc.* **2015**, *137*, 3638–3648.

(8) Wang, J.; Ji, L.; Chen, Z. In Situ Rapid Formation of a Nickel-Iron-Based Electrocatalyst for Water Oxidation. *ACS Catal.* **2016**, *6*, 6987–6992.

(9) Choi, W.; Manthiram, A. Comparison of metal ion dissolutions from lithium ion battery cathodes. *J. Electrochem. Soc.* **2006**, *153*, A1760.

(10) Gilbert, J. A.; Shkrob, I. A.; Abraham, D. P. Transition Metal Dissolution, Ion Migration, Electrocatalytic Reduction and Capacity Loss in Lithium-Ion Full Cells. *J. Electrochem. Soc.* **2017**, *164*, A389–A399.

(11) Leung, K. First-Principles Modeling of Mn(II) Migration above and Dissolution from LixMn2O4 (001) surfaces. *Chem. Mater.* **2017**, *29*, 2550–2562.

(12) Cornell, R. M.; Schwertmann, U. *The Iron Oxides: Structure, Properties, Reactions, Occurrences and Uses*; John Wiley & Sons, 2003.

(13) Handler, R. M.; Beard, B. L.; Johnson, C. M.; Scherer, M. M. Atom exchange between aqueous Fe (II) and goethite: an Fe isotope tracer study. *Environ. Sci. Technol.* **2009**, *43*, 1102–1107.

(14) Yanina, S. V.; Rosso, K. M. Linked reactivity at mineral-water interfaces through bulk crystal conduction. *Science* **2008**, *320*, 218–222.

(15) Joshi, P.; Gorski, C. A. Anisotropic morphological changes in goethite during Fe2+-catalyzed recrystallization. *Environ. Sci. Technol.* **2016**, *50*, 7315–7324.

(16) Zarzycki, P.; Rosso, K. M. Stochastic Simulation of Isotopic Exchange Mechanisms for Fe(II)-Catalyzed Recrystallization of Goethite. *Environ. Sci. Technol.* **2017**, *51*, 7552–7559.

(17) Stack, A. G.; Raiteri, P.; Gale, J. D. Accurate rates of the complex mechanisms for growth and dissolution of minerals using a combination of rare-event theories. *J. Am. Chem. Soc.* **2011**, *134*, 11–14.

(18) De La Pierre, M.; Raiteri, P.; Stack, A. G.; Gale, J. D. Uncovering the Atomistic Mechanism for Calcite Step Growth. *Angew. Chem., Int. Ed.* **2017**, *56*, 8464–8467.

(19) Du, J.; Rimsza, J. M. Atomistic computer simulations of water interactions and dissolution of inorganic glasses. *npj Mater. Degrad.* **2017**, *1*, 16.

(20) Benedek, R.; Thackeray, M. M.; Low, J.; Bučko, T. Simulation of Aqueous Dissolution of Lithium Manganate Spinel from First Principles. *J. Phys. Chem. C* **2012**, *116*, 4050–4059.

(21) Johnson, D. B.; Hallberg, K. B. Carbon, Iron and Sulfur Metabolism in Acidophilic Micro-Organisms. *Adv. Microb. Physiol.* **2008**, *54*, 201–255.

(22) Johnson, D. B.; Kanao, T.; Hedrich, S. Redox transformations of iron at extremely low pH: fundamental and applied aspects. *Front. Microbiol.* **2012**, *3*, 96.

(23) Zinder, B.; Furrer, G.; Stumm, W. The coordination chemistry of weathering: II. Dissolution of Fe (III) oxides. *Geochim. Cosmochim. Acta* **1986**, *50*, 1861–1869.

(24) Cheng, T.; Xiao, H.; Goddard, W. A., III Free-energy barriers and reaction mechanisms for the electrochemical reduction of CO on the Cu (100) surface, including multiple layers of explicit solvent at pH 0. *J. Phys. Chem. Lett.* **2015**, *6*, 4767–4773.

(25) Klyukin, K.; Alexandrov, V. CO2 Adsorption and Reactivity on Rutile TiO2(110) in Water: An Ab Initio Molecular Dynamics Study. *J. Phys. Chem. C* **2017**, *121*, 10476–10483.

(26) Russell, B.; Payne, M.; Ciacchi, L. C. Density functional theory study of Fe (II) adsorption and oxidation on goethite surfaces. *Phys. Rev. B: Condens. Matter Mater. Phys.* **2009**, *79*, 165101.

(27) Alexandrov, V.; Rosso, K. M. Ab initio modeling of Fe(II) adsorption and interfacial electron transfer at goethite (alpha-FeOOH) surfaces. *Phys. Chem. Chem. Phys.* **2015**, *17*, 14518–14531.

(28) Alexandrov, V.; Rosso, K. M. Electron transport in pure and substituted iron oxyhydroxides by small-polaron migration. *J. Chem. Phys.* **2014**, *140*, 234701.

(29) Kresse, G.; Furthmüller, J. Efficient iterative schemes for ab initio total-energy calculations using a plane-wave basis set. *Phys. Rev. B: Condens. Matter Mater. Phys.* **1996**, *54*, 11169.

(30) Leung, K.; Criscenti, L. J. Predicting the acidity constant of a goethite hydroxyl group from first principles. *J. Phys.: Condens. Matter* **2012**, *24*, 124105.

(31) Nosé, S. A molecular dynamics method for simulations in the canonical ensemble. *Mol. Phys.* **1984**, *52*, 255–268.

(32) Hoover, W. G. Canonical dynamics: equilibrium phase-space distributions. *Phys. Rev. A: At., Mol, Opt. Phys.* **1985**, *31*, 1695.

(33) *Understanding Molecular Simulation*, 2nd ed.; Frenkel, D., Smit, B., Eds.; Academic Press: San Diego, 2002; pp 525–532.

(34) Pinney, N.; Kubicki, J. D.; Middlemiss, D. S.; Grey, C. P.; Morgan, D. Density Functional Theory Study of Ferrihydrite and Related Fe-Oxyhydroxides. *Chem. Mater.* **2009**, *21*, 5727–5742.

(35) Zarzycki, P.; Kerisit, S.; Rosso, K. M. Molecular Dynamics Study of Fe(II) Adsorption, Electron Exchange, and Mobility at Goethite (alpha-FeOOH) Surfaces. *J. Phys. Chem. C* **2015**, *119*, 3111–3123.

(36) Zarzycki, P.; Rosso, K. M. Stochastic Simulation of Isotopic Exchange Mechanisms for Fe(II)Catalyzed Recrystallization of Goethite. *Environ. Sci. Technol.* **2017**, *51*, 7552–7559.

(37) Leung, K.; Criscenti, L. J. Lead and selenite adsorption at water–goethite interfaces from first principles. *J. Phys.: Condens. Matter* **2017**, *29*, 365101.

(38) Kubicki, J. D.; Tunega, D.; Kraemer, S. A density functional theory investigation of oxalate and Fe (II) adsorption onto the (010) goethite surface with implications for ligand-and reduction-promoted dissolution. *Chem. Geol.* **2017**, *464*, 14–22.

(39) Rong, X.; Kolpak, A. M. Ab Initio Approach for Prediction of Oxide Surface Structure, Stoichiometry, and Electrocatalytic Activity in Aqueous Solution. *J. Phys. Chem. Lett.* **2015**, *6*, 1785–1789.

(40) Brennan, E. W.; Lindsay, W. L. Reduction and oxidation effect on the solubility and transformation of iron oxides. *Soil Sci. Soc. Am. J.* **1998**, *62*, 930.

(41) Rueda, E. H.; Ballesteros, M. C.; Grassi, R. L.; Blesa, M. A. Dithionite as a dissolving reagent for goethite in the presence of EDTA and citrate. Application to soil analysis. *Clays Clay Miner.* **1992**, *40*, 575.

(42) Sidhu, P. S.; Gilkes, R. J.; Cornell, R. M.; Posner, A. M.; Quirk, J. P. Dissolution of iron oxides and oxyhydroxides in hydrochloric and perchloric acids. *Clays Clay Miner.* **1981**, *29*, 269–276.

(43) Cornell, R. M.; Posner, A. M.; Quirk, J. P. Kinetics and mechanisms of the acid dissolution of goethite (α-FeOOH). *J. Inorg. Nucl. Chem.* **1976**, *38*, 563–567.